metals

Article

Complex Precipitates of TiN-MC$_x$ in GCr15 Bearing Steel

Qianren Tian [1], Guocheng Wang [1,2,3,*], Xinghu Yuan [1], Qi Wang [1,2] and Seetharaman Sridhar [3]

[1] School of Materials and Metallurgy, University of Science and Technology Liaoning, Anshan 114051, China; tianqianren@126.com (Q.T.); 18341263233@163.com (X.Y.); wangqi8822@sina.com (Q.W.)

[2] Key Laboratory of Chemical Metallurgy Engineering Liaoning Province, University of Science and Technology Liaoning, Anshan 114051, China

[3] Department of Metallurgical and Materials Engineering, Colorado School of Mines, Golden, CO 80401, USA; sseetharaman@mines.edu

* Correspondence: wang_guocheng@163.com

Received: 7 May 2019; Accepted: 31 May 2019; Published: 3 June 2019

Abstract: Nitride and carbide are the second phases which play an important role in the performance of bearing steel, and their precipitation behavior is complicated. In this study, TiN-MC$_x$precipitations in GCr15 bearing steels were obtained by non-aqueous electrolysis, and their precipitation mechanisms were studied. TiN is the effective heterogeneous nucleation site for Fe_7C_3 and Fe_3C; therefore, MC$_x$can precipitate on the surface of TiN easily. The chemistry component of MC$_x$ consists of M_3C and M_7C_3 (M = Fe, Cr, Mn) and Cr_3C_2. TiN-MC$_x$ with high TiN volume fraction, TiN forms in early stage of solidification, and MC$_x$ precipitates on TiN surface after TiN engulfed by the solidification advancing front. TiN-MC$_x$ with low TiN volume fraction, TiN and MC$_x$ form in late stage of solidification, TiN can not grow sufficiently and is covered by numerous precipitated MC$_x$particles.

Keywords: non-aqueous electrolysis; TiN-MC$_x$; precipitation; bearings; high carbon chromium bearing steel

1. Introduction

Controlling microstructures and second phase in steel plays a vital role in the quality of steel. Carbide (M_3C, M_3C_2, M_7C_3, M = Fe, Cr, Mn) [1,2] and TiN inclusion [3,4] are common second phases in high carbon chromium steel. As a result of good wear resistance and solid solubility with alloy elements (Cr, Mn) [5,6], carbide can retain good mechanical properties of bearing steel during heat treatment [7,8]. Recently, utilization of inclusions has become attractive to improve steel performance. TiN is more harmful to bearing steel than Al_2O_3 in the same size [9]. Many studies have investigated TiN and Al_2O_3, $MgAl_2O_4$ and MnS, and NbC complex precipitation with inclusion [10–13]. Our previous study [14] found that TiN inclusion was covered by carbide in the etched GCr15 bearing steel metallographic specimens. It is necessary to observe their three-dimensional (3-D) morphologies in steel because the two-dimensional (2D) nature of the particles cannot reflect their real morphologies.

The non-aqueous electrolysis extraction of second phase from steel is an effective method to study its 3D morphologies and composite interfaces. Fang and Ni [15] studied the behaviors of rare earth dissolved in α-Fe, Fe-Ce intermetallic compounds and rare earth inclusions via non-aqueous electrolysis. Bi et al. [16] analyzed 3D morphology, quantity, and chemistry of inclusion in ferroalloys by the electrolysis method. Wang et al. [17] observed Al_2O_3-MnO-SiO_2(-MnS) inclusion in steel by non-aqueous electrolysis. Zhang et al. [18,19] analyzed Ca-Mg spinel in cord steel and MnS in heavy rail steel by the electrolysis. Zhang et al. [20] studied the suitable electrolytic conditions for 16MnCrS5 steel.

In this study, 3D morphologies of the carbide (MC$_x$, M = Fe, Cr, Mn) and TiN-MC$_x$ precipitates extracted from GCr15 bearing steel specimens by the non-aqueous electrolysis were observed by field emission scanning electron microscope-energy dispersive spectrometer (FESEM-EDS). The MC_x chemistry component was confirmed by X-ray diffraction (XRD) and FactSage^{TM} phase diagram calculation. The precipitation mechanism of TiN-MC_x with different volume fraction in GCr15 bearing steels was elucidated.

2. Experiment

2.1. Chemical Components Analysis

The chemical compositions of GCr15 bearing steel produced by the basic oxygen furnace (BOF)-landle furnace (LF)-vacuum degas (VD)-continuous casting (CC) process in a foundry were determined by direct-reading spectrometer (Model: ARL-3460 Optical Emission Spectrometer, Thermo Fisher Corporation, Waltham, MA, USA). The total oxygen and total nitrogen contents were analyzed using a nitrogen-oxygen analyzer (Model: TC-600, LECO Corporation, St. Joseph, MI, USA). The chemical compositions of the GCr15 bearing steel are shown in Table 1.

Table 1. Chemical Compositions of GCr15 Bearing Steel (in mass percent).

Composition	C	Si	Mn	P	S	Ti	Cr	V	N	Alt	Ca	O (T)
Concentration	1.01	0.25	0.36	0.012	0.0014	0.0078	1.46	0.0099	0.0049	0.012	<0.005	0.0009

2.2. Non-Aqueous Electrolysis and XRD Detection

The non-aqueous electrolysis method was used to extract TiN-MC_x particles from the GCr15 bearing steel. Samples with diameter of 10 mm and height of 100 mm were used as anode and copper as cathode. The electrolyte consists of 1% tetramethylammonium chloride, 5% triethanolamine, 5% glycerol, and 89% anhydrous methanol (in volume percentage). The constant voltage direct current (DC) power supply (model: DH1720A-1) was used to keep the current density between 40–60 mA/cm^2. The temperature of the electrolyte was kept at 268–278 K (−5–5 °C). Argon gas was used to stir organic electrolyte. After electrolysis, steel samples were placed in a beaker containing ethanol and vibrated with ultrasonic wave to separate all particles from the samples surface. MC_x and inclusions in ethanol were further separated by the magnetism. The inclusion particles were transferred directly to the double-sided carbon bands attached to the conductive material and then were observed by FESEM-EDS. After magnetic separation, MC_x was analyzed by XRD (Model: X'Pert Powder, Malvern PANalytic Ltd., Malvine, UK, the detection parameters are that Cu $K\alpha\lambda = 0.154178$ nm, tube current 40 mA and tube voltage 40 kV, scanning scope 30–85 °C, step length 0.013 s, residence time 5 s).

3. Result

3.1. Observation for Particles

2D morphologies of TiN-MC_x in the metallographic specimens etched by 4% nitric acid alcohol were observed by FESEM-EDS and are shown in Figure 1. The EDS points are the black crosses, and the analysis for elements can both be seen in Figure 1. The dark grey particles are TiN inclusions, and the light grey particles are MC_x. Figure 1a shows a long strip and large size TiN with a small amount of MC_x around it. Figure 1b–d show TiN with less pronounced aspect ratios and it is covered by a larger number of MC_x, which, in some cases, form a continuous layer rather than discrete particles.

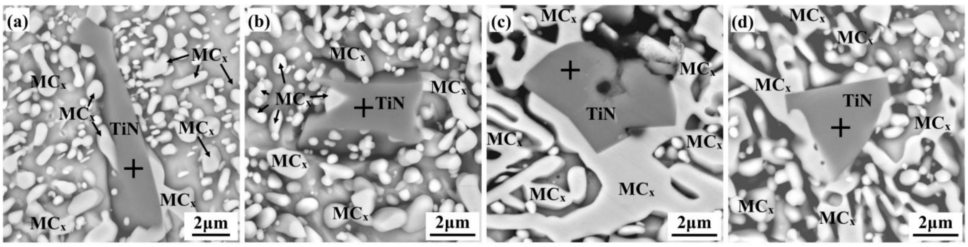

No.	EDS point analysis (element in atomic percentage)				
	Ti	N	V	Cr	Fe
(a)	54.78	34.91	2.65	6.20	1.46
(b)	53.89	41.05	1.27	2.36	1.42
(c)	40.28	44.95	2.45	7.56	4.12
(d)	46.09	46.02	2.43	4.12	1.34

Figure 1. TiN-MC$_x$particles and energy dispersive spectrometer (EDS) point analysis for TiN part in etched metallographic specimens. (**a**) Long-strip and large size TiN with MC$_x$; (**b**)–(**d**) small size TiN with MC$_x$.

3D morphologies, chemistries of TiN-MC$_x$ and EDS point analysis for TiN part were also observed by FESEM-EDS; the atomic percentage of element can be seen in each element mapping. Figure 2a shows TiN-MC$_x$with large size TiN inclusion (in comparison to MC$_x$) whose size was approximately 25 μm. This category of TiN-MC$_x$ is denoted as "TiN-MC$_x$ with high TiN volume fraction". The elements mapping shows that Ti and V can form the solid solution; however, the metallic elements in MC$_x$ are Fe and Cr. Mn cannot be detected because of its low content. Figure 2b shows that TiN-MC$_x$ with small size TiN are approximately 5 μm, with its shape more closely resembling a sphere. In comparison with the TiN-MC$_x$ in Figure 2a, TiN in the precipitates is clearly smaller. This category of TiN-MC$_x$ is denoted as "TiN-MC$_x$ with low TiN volume fraction". The TiN-MC$_x$ with low TiN volume fraction is almost completely covered by MC$_x$.

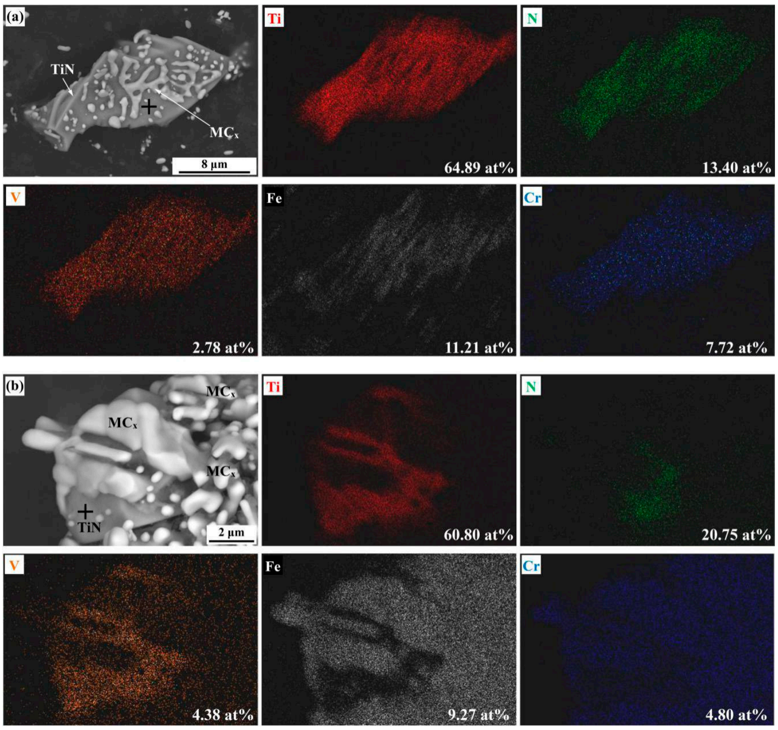

Figure 2. Morphologies and elements mapping of TiN-MC$_x$ and EDS point analysis for TiN part. (**a**) High TiN volume fraction; (**b**) low TiN volume fraction.

Figure 3 shows the 3D morphologies of MC_x and elements mapping of Fe, Cr, and Mn. The morphologies of single MC_x particles are not significantly different from that of MC_x on the surface of TiN inclusion. Figure 3a shows a spherical $MC_x$with a smaller size, less 1 µm. Figure 3b shows a flat MC_x with approximately 1 µm, whereas a MC_x with a shape of a long strip of length 6 µm can be seen in Figure 3c, which is rarely found in steel. Figure 3d shows MC_x transferred on the conductive carrier, and the MC_x are predominantly spherical and flat. Figure 3e,f are cluster-like MC_x, with Fe, Cr and Mn elements mapping results. The size of cluster-like MC_x are approximately 15 µm. However, the cluster-like MC_x exhibits the morphology of banded or reticulated MC_xin metallographic samples. In Figure 3e,f, C is not shown because MC_x and inclusions were transferred on the carbon bands.

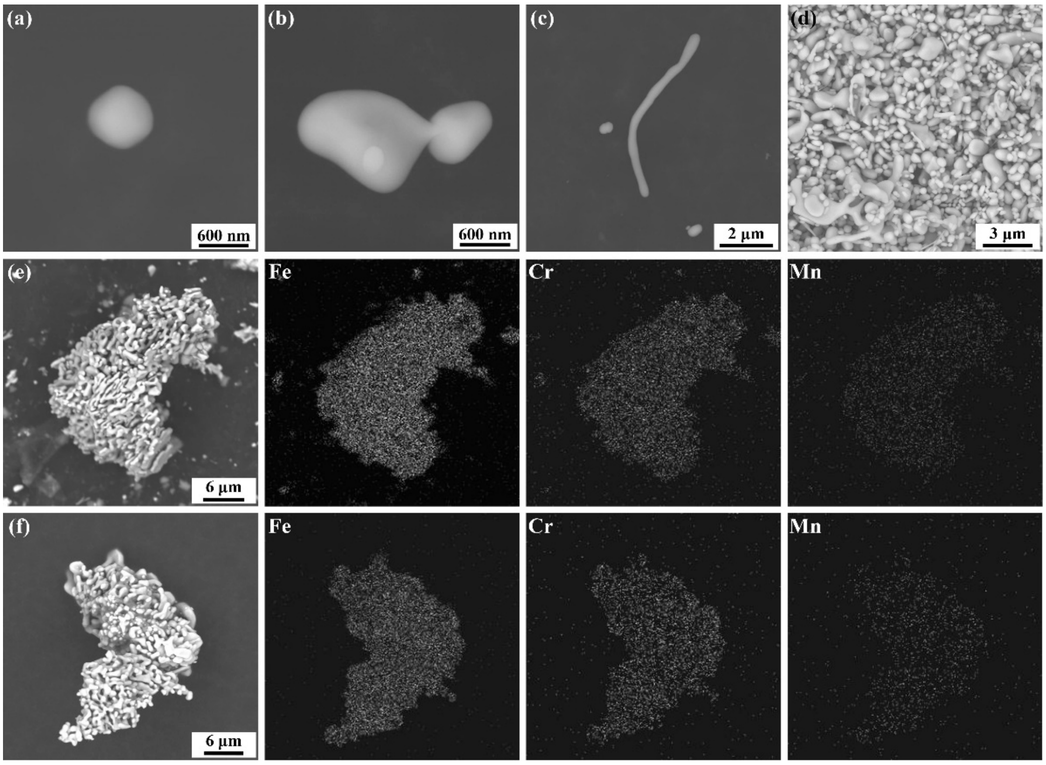

Figure 3. Morphologies and elements mapping of MC_x. (**a**) Ball-like MC_x; (**b**) flat-like MC_x; (**c**) long stripe-like; (**d**) MC_x transferred on the conductive carrier; (**e**) and (**f**) cluster-like MC_x with elements mapping of Fe, Cr, and Mn.

3.2. *XRD Result*

Figure 4 shows the result of the MC_x XRD experiment; the structures of the MC_x are predominantly M_3C and M_7C_3, with M_3C as the dominant carbide. At 2θ = 48.6°, several Cr_3C_2 remained. The results are similar to carbides in GCr15 bearing steel after electroslag remelting-continuous casting (ESR-CC) process, as demonstrated by Du et al. [2] The main MC_x in that study were M_3C, M_3C_2, and M_7C_3, and the content of Cr in their sample was 1.47% and 0.31% [2], respectively, which is similar to that seen in our steel.

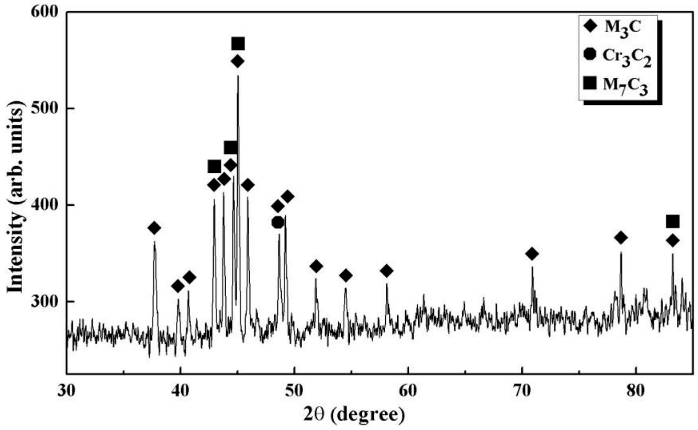

Figure 4. XRD analysis result of the extracted MC_x in the GCr15 bearing steel.

4. Discussion

4.1. Thermodynamic Analysis

The phase diagram of Fe-1.5%Cr-C system was calculated via FactSage^{TM} 7.2 thermodynamic software and steel database [21]. The calculated phase diagram for the conditions, [pct Cr] = 1.5, [pct C] = 0.5–1.5 ([pct element] is mass percent of the element in steel), and the temperature range from 298 K (25 °C) to 1873 K (1600 °C), is shown in Figure 5 and the gray part presents the mushy zone of steel. When [pct C] = 1, equilibrium transformation of steel is that liquid → FCC + liquid → FCC → M_3C + FCC → M_3C + FCC + BCC → M_3C + BCC → C + M_3C + BCC → C + BCC + M_7C_3 → C + BCC + Cr_3C_2. The liquidus temperature and solidus temperature are close to the calculated values in our previous paper [liquidus and solidus temperature are 1723 K (1450 °C) and 1601 K (1328 °C), respectively] [14]. When the temperature is slightly lower than 1173 K (900 °C), M_3C gradually precipitates from FCC phase; when the temperature is approximately 913 K (640 °C), M_3C gradually transforms to M_7C_3. When the temperature is slightly higher than 773 K (500 °C), the carbide gradually transforms into Cr_3C_2. During this process, phase transformation will be difficult to be completed to the phase fraction, dictated by the equilibrium phase diagram which leads to the transition layers. The main phases formed during temperature gradual decreasing are M_3C, M_7C_3, Cr_3C_2, and their content decreases in turn. FactSage^{TM} calculation results are consistent with XRD results, in which MC_x were found to be M_3C, M_7C_3, and Cr_3C_2.

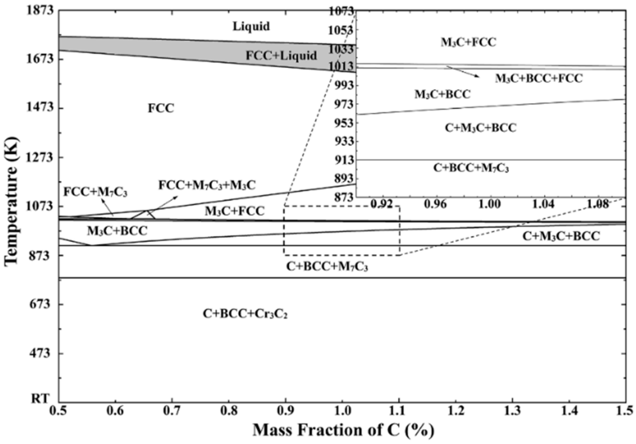

Figure 5. Phase diagram for Fe-1.5%Cr-C system (the shadow part is the mushy zone of steel, C presents the pure substance C(s); M_3C (Cementite) presents Fe_3C with dissolved Cr, Mn; M_7C_3 presents carbide phase found in Cr, Mn-containing steels; FCC and BCC present the face-centered cubic iron (γ-Fe) and body-centered cubic iron (α-Fe), respectively).

As demonstrated in previous work [14,22], TiN precipitates in the mushy zone of GCr15 bearing steel, and their size is affected by the concentration of Ti and N around TiN crystal nucleus. Ti and N both are positive segregation elements ($k > 0$), their concentrations and, consequently, the supersaturation increases with an increase in solid fraction, and TiN precipitation become easier during solidification process. Recently, Li et al. [23] studied the precipitation of TiN inclusions in GCr15 bearing steel during solidification by calculating the thermodynamics and growth kinetics in consideration of solidification segregation of the solute elements. They believe that the effect of Ti content on the size of TiN inclusions is greater than that of N content.

Fe, Cr, Mn, and C can precipitate on TiN, which is the heterogeneous nucleation site for MC_x. It can be seen in Figure 2a that the size of TiN is large and, consequently, TiN would be formed at the early stage of solidification and has enough time to grow. TiN in Figure 2b precipitates at the late stage of solidification. The diffusion coefficients D_i, i = Cr, Ti, Mn, C, N in γ-phase were calculated according to the phase diagrams, when [pct C] = 1 and FCC precipitates at 1673 K (1400 °C). The relationship between diffusion coefficients and temperature from 1673 to 1173 K (1400 to 900 °C) is shown in Figure 6a, and the parameters are shown in Table 2. From Figure 6a, in 1673–1642 K (1400–1369 °C), $\mathrm{D}_{\mathrm{N}}^{\gamma} > \mathrm{D}_{\mathrm{C}}^{\gamma} > \mathrm{D}_{\mathrm{Ti}}^{\gamma} > \mathrm{D}_{\mathrm{Mn}}^{\gamma} > \mathrm{D}_{\mathrm{Cr}}^{\gamma}$; in 1642–1173 K (1369–900 °C), $\mathrm{D}_{\mathrm{C}}^{\gamma} > \mathrm{D}_{\mathrm{N}}^{\gamma} > \mathrm{D}_{\mathrm{Ti}}^{\gamma} > \mathrm{D}_{\mathrm{Mn}}^{\gamma} > \mathrm{D}_{\mathrm{Cr}}^{\gamma}$. The results indicate that the diffusion of C and N plays a dominant role. The diffusion of C is more efficient than N after the temperature has decreased under 1642 K. In contrast, the diffusion of Cr, Ti, and Mn are extremely small in γ-phase; the content of Cr is much larger than that of Mn and Ti, which would not affect the precipitation of MC_x. That indicates that TiN may precipitate more easily in the range of temperature of 1673 K–1642 K in comparison with MC_x, which precipitates easily during the following decreasing temperature process.

Table 2. Diffusion coefficient and equilibrium partition coefficient of C, Cr, Mn, Ti, and N in γ-phase. Data from [3,24–26].

Element	Equilibrium Partition Coefficient, k	Diffusion Coefficient in γ-phase (cm^2/s)
C	0.34	0.0761·EXP (−134600/RT)
Cr	0.85	0.0012·EXP (−219000/RT)
Mn	0.78	0.486·EXP (−276100/RT)
Ti	0.33	0.15·EXP (−251000/RT)
N	0.48	0.91·EXP (−168500/RT)

The segregation degree of C, Cr, Ti, Mn, and N during solidification is calculated according to Equations (1) to (5) [27] in Figure 6b, at cooling rate of 0.5 K/s, temperature of 1723 K to 1601 K (1450 °C to 1328 °C) and corresponding solid fraction is 0–1. The order of segregation from high to low is Ti, C, N, Mn, and Cr at the same solid fraction. The segregation degree of C at the late stage of solidification reaches tens of times the initial content. Therefore, $\mathrm{MC_x}$ precipitation on the TiN surface becomes easier at the late stages of solidification.

$$\frac{[\mathrm{pct\,X}]_{\mathrm{t}}}{[\mathrm{pct\,X}]_{0}} = \left[1 - \left(1 - \frac{\beta k_i}{1+\beta}\right) \cdot f_s\right]^{\frac{k_i - 1}{1 - \frac{\beta k_i}{1+\beta}}} \tag{1}$$

$$\beta = \frac{4D_i^{\gamma}}{L^2} \tag{2}$$

$$\tau = \frac{\mathrm{T_l} - \mathrm{T_s}}{\mathrm{R_c}} \tag{3}$$

$$L = 143.9 \times \mathrm{R_c}^{-0.386}, \left([\mathrm{pctC}] = 1\right) \tag{4}$$

$$\mathrm{T} = \mathrm{T_{Fe}} - \frac{\mathrm{T_{Fe}} - \mathrm{T_l}}{1 - f_{\mathrm{s}} \frac{\mathrm{T_l} - \mathrm{T_s}}{\mathrm{T_{Fe}} - \mathrm{T_s}}} \tag{5}$$

Here, $[\text{pct X}]_t$is the C concentration at solidification front, $[\text{pct X}]_0$ is the initial C concentration; f_s is solid fraction; k_i is equilibrium distribution coefficient of C, Cr, Mn, Ti, and N in γ-phase; D_i^{γ} is diffusion coefficient of C, Cr, Mn, Ti, and N in γ-phase, cm^2/s; τ is the local cooling time, s; R_c is the local cooling rate, K/s; L is secondary arm space, μm; T_{Fe}, T_l, and T_s are the melting point of pure iron [1809 K (1536 °C)], the liquidus temperature [1723 K (1450 °C)], and the solidus temperature [1601 K (1328 °C)] of GCr15 steel [14], respectively.

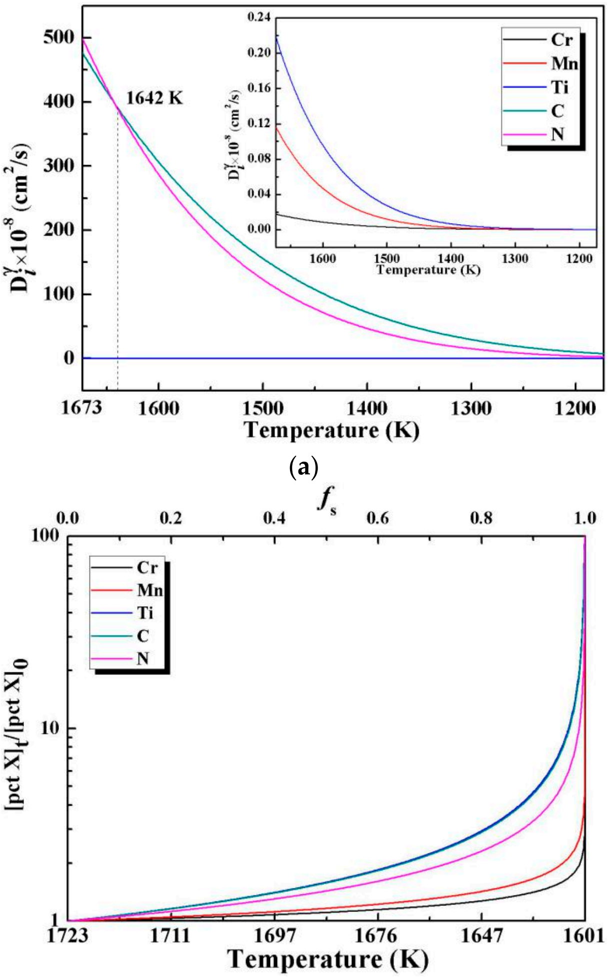

(**a**)

(**b**)

Figure 6. Diffusion coefficient change in γ-phase and segregation degree of C, Mn, Ti, C, N during solidification process (**a**) diffusion coefficient change; (**b**) segregation degree.

4.2. Crystallographic Analysis

Using the disregistry theory [28,29], the inconsistency of lattice parameters between matrix and nucleating phase can indicate the effectiveness of nucleating catalysts. Choosing three crystal planes and three crystal orientations of the matrix and new phase crystal, the corresponding crystal parameters can calculate the disregistries between two phases by Equation (6). Because M_3C and M_7C_3 are substitutional solid solutions (Cr and Mn take the position of Fe in carbides) [30], the minimum disregistries of TiN-M_7C_3, TiN-M_3C, and Fe_3C-Fe_7C_3 were verified by the parameters of TiN [14], Fe_7C_3 [31] and Fe_3C [32]. The parameters and calculated results are shown in Table 3, and the disregistries diagram is shown in Figure 7. The disregistry between $[\bar{1}11]$ (110)TiN|| $[\bar{1}11]$ (110)Fe_7C_3, $[\bar{1}11]$ (110)TiN|| $[\bar{1}11]$ (110)Fe_3C and [011](100)Fe_3C||[011](100)Fe_7C_3 is 1.49%, 5.16% and 7.40%, respectively. The results show that the disregistries between TiN and Fe_7C_3 and Fe_3C are both small; consequently, TiN would provide suitable heterogeneous nucleation sites for Fe_7C_3 and Fe_3C.

$$\delta^{(hkl)_\mathrm{s}}_{(hkl)_\mathrm{n}} = \frac{1}{3}\sum_{i=1}^{3}\frac{\left|\left(d_{[uvw]^{\mathrm{i}}_{\mathrm{s}}}\cdot\cos\theta\right) - d_{[uvw]^{\mathrm{i}}_{\mathrm{n}}}\right|}{d_{[uvw]^{\mathrm{i}}_{\mathrm{n}}}} \times 100\% \tag{6}$$

where $\delta^{(hkl)_s}_{(hkl)_n}$ is disregistry between a solid plane $(hkl)_\mathrm{s}$ and a nucleate plane $(hkl)_\mathrm{n}$; $d_{[uvw]^{\mathrm{i}}_{\mathrm{s}}}$ and $d_{[uvw]^{\mathrm{i}}_{\mathrm{n}}}$ are the interatomic spacing along a low-index direction $[uvw]_\mathrm{s}$ and the interatomic spacing along a low-index direction $[uvw]_\mathrm{n}$; θ is the angle between $[uvw]_\mathrm{s}$ and $[uvw]_\mathrm{n}$.

Table 3. Parameters and lattice disregistry between tin and nucleation phase.

Substance (Space Group)	**Lattice Parameters (Length Unit: Å)**					
Fe_7C_3 (Pnma) [31]	**a**	**b**	**C**	**α = β = γ (°)**		
	4.537	6.892	11.913	90		
TiN-Fe_7C_3	$[hkl]_s$	$[hkl]_n$	$d_{[hkl]_s}$	$d_{[hkl]_n}$	θ (°)	Disregistry
(100)TiN‖(100)Fe_7C_3	[001]	[001]	2.118	11.913	0(-)	
	[011]	[011]	2.995	13.763	14.949	6.52%
	[010]	[010]	2.118	6.892	-	
(110)TiN‖(110)Fe_7C_3	$[\bar{1}10]$	[001]	2.995	11.913	-	
	$[\bar{1}11]$	$[\bar{1}11]$	3.668	14.492	0.556	1.49%
	[001]	$[\bar{1}10]$	2.118	8.251	-	
(111)TiN‖(111)Fe_7C_3	$[0\bar{1}1]$	$[0\bar{1}1]$	2.995	13.763	5.275	
	$[\bar{1}01]$	$[\bar{1}01]$	2.995	12.748	18.715	8.93%
	$[\bar{1}10]$	$[\bar{1}10]$	2.995	8.251	-	
Substance (Space Group)	**Lattice Parameters (Length Unit: Å)**					
Fe_3C (Pnma) [32]	**a**	**b**	**C**	**α = β = γ (°)**		
	5.092	6.741	4.527	90		
TiN-Fe_3C	$[hkl]_s$	$[hkl]_n$	$d_{[hkl]_s}$	$d_{[hkl]_n}$	θ (°)	Disregistry
(100)TiN‖(100)Fe_3C	[001]	[001]	2.118	4.527	-	
	[011]	[011]	2.995	8.120	11.116	6.92%
	[010]	[010]	2.118	6.741	-	
(110)TiN‖(110)Fe_3C	$[\bar{1}10]$	$[\bar{1}10]$	2.995	8.448	-	
	$[\bar{1}11]$	$[\bar{1}11]$	3.668	9.585	26.551	5.16%
	[001]	[001]	2.118	4.527	-	
(111)TiN‖(111)Fe_3C	$[0\bar{1}1]$	$[0\bar{1}1]$	2.995	8.448	3.227	
	$[\bar{1}01]$	$[\bar{1}01]$	2.995	8.120	8.258	9.25%
	$[\bar{1}10]$	$[\bar{1}10]$	2.955	6.813	-	
Fe_3C-Fe_7C_3	$[hkl]_s$	$[hkl]_n$	$d_{[hkl]_s}$	$d_{[hkl]_n}$	θ (°)	Disregistry
(110)Fe_3C‖(110)Fe_7C_3	[001]	[001]	4.527	11.913	-	
	$[\bar{1}11]$	$[\bar{1}11]$	9.585	14.492	27.107	11.38%
	$[\bar{1}10]$	$[\bar{1}10]$	8.448	8.251	-	
(100)Fe_3C‖(100)Fe_7C_3	[001]	[001]	4.527	11.913	-	-
	[011]	[011]	8.120	13.763	26.068	7.40%
	[010]	[010]	6.741	6.892	-	-
(111)FeC_3‖(111)Fe_7C_3	$[\bar{1}01]$	$[0\bar{1}1]$	8.120	13.763	2.983	
	$[0\bar{1}1]$	$[\bar{1}01]$	8.448	12.748	15.488	21.0%
	$[\bar{1}10]$	$[\bar{1}10]$	6.813	8.251	-	

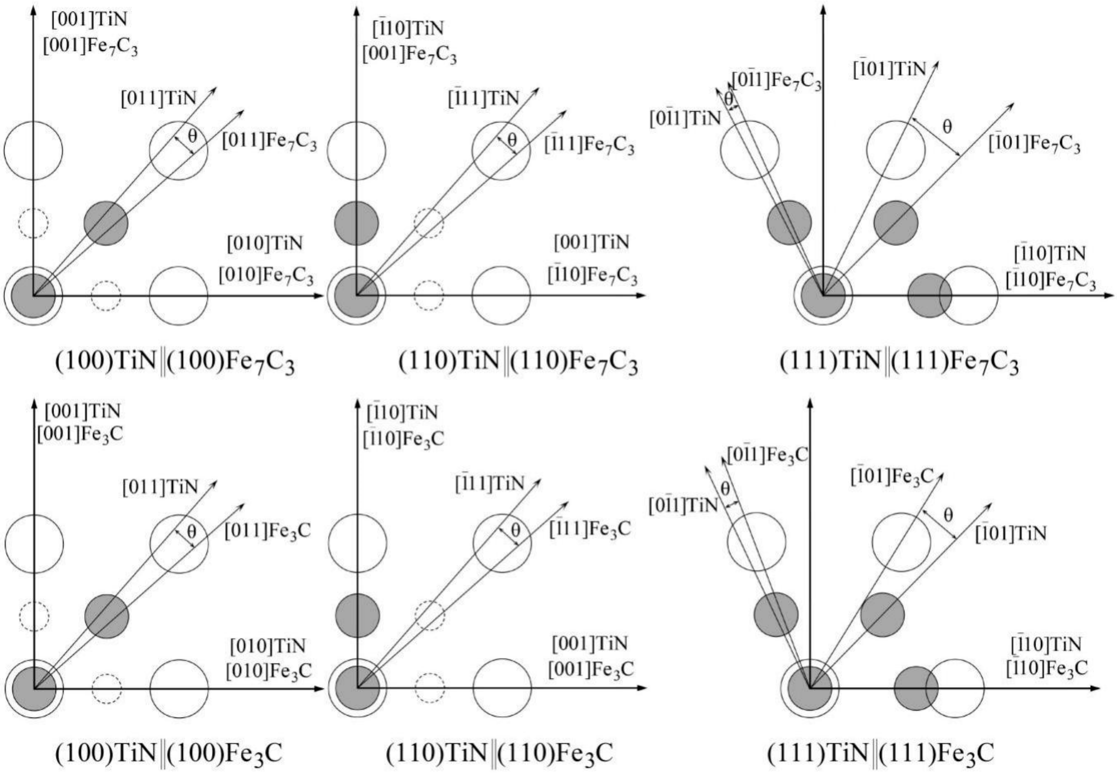

Figure 7. Schematic diagram of disregistry between TiN and FeC_x (x = 3/7, 1/3).

4.3. *Pushing and Engulfment Behavior of Particles*

Descotes et al. [33] found that TiN particles could be engulfed by the solid side at the solid-liquid interface in the solidification process. However, Pervushuin et al. [34] reported that TiN was pushed into the liquid side in molten steel during solidification. In our previous study [22], the local cooling rate and movement velocity of solidification front were confirmed as 0.7 K/s and 3 μm/s by the observation of confocal laser scanning microscope (CLSM), respectively. The changes of temperature, time, and distance are approximately 7 K, 10.6 s, and 32 μm, as shown in Figure 8. The critical velocity of pushing or engulfment $V_{cr} = 23/R$ (R is the radius for globular particles) [35], when R is 12.5 μm and 2.5 μm (the particles in Figure 2), V_{cr} are equal to 1.84 μm/s and 9.2 μm/s, respectively. This indicates that the large size TiN inclusion is easier to be engulfed than small size TiN. In the actual process, the local cooling rate is 0.5 to 10 K/s. The higher the local cooling rate is, the faster the solidification front moves, and the more easily the inclusions are engulfed.

The size of TiN-MC_x is larger than TiN, TiN-MC_{x} moves more slowly than TiN, and is easier to be swallowed by the solidification front. After the engulfment, particles will continue to grow through solid state diffusion, the rate of which will decrease with decreasing temperature. For TiN-MC_{x} pushed to the liquid phase, elements segregation provides the possibility for the growth of MC_x on TiN, TiN-MC_x growing until its size is large enough to be engulfed by the solid phase. The precipitation mechanism of TiN-MC_x in different solidification periods can be confirmed.

- TiN-MC_x with high TiN volume fraction precipitates at the early stage of solidification and has better growth kinetics in the melt. After being engulfed by the solidification front, MC_x grows at a lower rate on the surface of TiN.
- TiN-MC_x with low TiN volume fraction precipitates in the late stage of solidification and does not have enough time to grow to large size. Due to high C concentration and segregation, a large amount of MC_x precipitates on TiN surface. When TiN-MC_x is large enough and engulfed by the solidification front, the volume fraction of MC_x is large enough to cover the TiN particle.

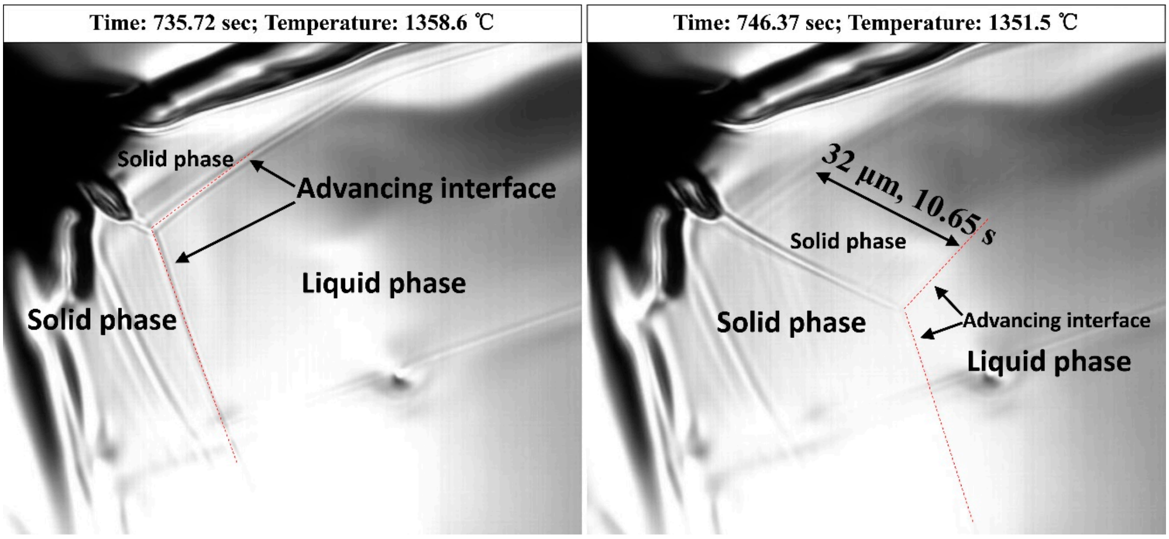

Figure 8. Parameters and distance changes of solidification front in GCr15 bearing steel.

5. Conclusions

In this study, TiN-MC_x precipitation mechanism in GCr15 bearing steels were analyzed by combining the experiments of non-aqueous electrolysis, FESEM observation with EDS and XRD analysis as well as with the theoretical analysis of thermodynamic and crystallographic analyses in addition to CLSM observation for pushing and engulfment behavior of particles. The main conclusions can be drawn:

(1) TiN-MC_xcomposed of TiN and MC_x, TiN is the effective heterogeneous nucleation site for Fe_7C3 and Fe_3C, in which the MC_x precipitates on the surface of TiN was observed in GCr15 bearing steel.

(2) MC_x(M = Fe, Cr, Mn) in GCr15 bearing steel smelted by converter is mainly composed of M_3C, M_7C_3, and Cr_3C_2.

(3) TiN-MC_x with high TiN volume fraction precipitates at the early solidification stage. After being engulfed by the solidification front, MC_x grows at a lower rate on the surface of TiN.

(4) TiN-$MC_x$with low TiN volume fraction precipitates in the late solidification stage and does not have enough time to grow to large size. When the size of TiN-MC_x is large enough and is engulfed by the solidification front, the volume fraction of MC_x is large enough to cover TiN particle because of high C concentration and segregation.

Author Contributions: Methodology, G.W. and X.Y.; Project administration, Q.W.; Supervision, G.W. and S.S.; Writing—original draft preparation, Q.T.; Writing—review and editing, Q.T.; Supervision, G.W.

Funding: This research was funded by National Natural Science Foundation of China (Grant Nos. 51874170 and 51634004).

Conflicts of Interest: The authors declare no conflict of interest.

References

1. Beswick, J.M. The effect of chromium in high carbon bearing steels. *Metall. Trans. A* **1987**, *18*, 1897–1906. [CrossRef]
2. Du, G.; Li, J.; Wang, Z.B. Control of carbide precipitation during electroslag remelting-continuous rapid solidification of GCr15 steel. *Metall. Mater. Trans. B* **2017**, *48*, 2873–2890. [CrossRef]
3. Yang, L.; Cheng, G.G.; Li, S.J.; Zhao, M.; Feng, G.P. Generation mechanism of TiN inclusion for GCr15SiMn during electroslag remelting process. *ISIJ Int.* **2015**, *55*, 1901–1905. [CrossRef]
4. Zhou, D.G.; Fu, J.; Chen, X.C.; Li, J. Precipitation behavior of TiN in bearing steel. *J. Mater. Sci. Technol.* **2003**, *19*, 184–186. [CrossRef]

5. Benz, R.; Elliott, J.F.; Chipman, J. Thermodynamics of the carbides in the system Fe-Cr-C. *Metall. Trans.* **1974**, *5*, 2235–2240. [CrossRef]
6. Benz, R.; Elliott, J.F.; Chipman, J. Thermodynamics of the solid phases in the system Fe-Mn-C. *Metall. Trans.* **1973**, *4*, 1975–1986. [CrossRef]
7. Krauss, G. *Principles of Heat Treatment of Steel*; ASM: Metals Park, OH, USA, 1980; pp. 222–224.
8. Monma, K.; Maruta, R.; Yamamoto, T.; Wakikado, Y. Role of spheroidized carbides on the fatigue life of bearing steel. *Jpn. Inst. Metall. J.* **1968**, *32*, 1198–1204. [CrossRef]
9. Fu, J.; Zhu, J.; Di, L.; Tong, F.; Liu, D.; Wang, Y. Study on the precipitation behavior of TiN in the microalloyed steels. *Acta Metall. Sin.* **2000**, *36*, 801–804.
10. Lee, M.H.; Park, J.H. Synergistic effect of nitrogen and refractory material on TiN formation and equiaxed grain structure of ferritic stainless steel. *Metall. Mater. Trans. B* **2018**, *49*, 877–893. [CrossRef]
11. Park, J.S.; Kim, D.H.; Park, J.H. TEM characterization of a TiN-$MgAl_2O_4$ epitaxial interface. *J. Alloys Comp.* **2017**, *695*, 476–481. [CrossRef]
12. Liu, Y.; Zhang, L.F.; Duan, H.J.; Zhang, Y.; Luo, Y.; Conejo, A.N. Extraction, thermodynamic analysis, and precipitation mechanism of MnS-TiN complex inclusions in low-sulfur steels. *Metall. Mater. Trans. A* **2016**, *47*, 3015–3025. [CrossRef]
13. Lee, Y.; Cooman, B.C.D. TiN/NbC compound particle formation during thin slab direct rolling of HSLA steel. *Steel Res. Int.* **2014**, *85*, 1158–1172. [CrossRef]
14. Tian, Q.R.; Wang, G.C.; Shang, D.L.; Lei, H.; Yuan, X.H.; Wang, Q.; Li, J. Precipitation behaviors of TiN inclusion in GCr15 bearing steel billet. *Metall. Mater. Trans. B* **2018**, *49*, 1149–1164. [CrossRef]
15. Fang, K.M.; Ni, R.M. Research on determination of the rare-earth content in metal phases of steel. *Metall. Trans. A* **1986**, *17*, 315–323.
16. Bi, Y.; Karasev, A.; Jönsson, P.G. Three-dimensional investigations of inclusions in ferroalloys. *Steel Res. Int.* **2014**, *85*, 659–669. [CrossRef]
17. Wang, G.C.; Li, S.L.; Ai, X.G.; Zhao, C.M.; Lai, C.B. Characterization and thermodynamics of Al_2O_3-MnO-SiO_2 (-MnS) inclusion formation in carbon steel billet. *J. Iron Steel Res. Int.* **2015**, *22*, 566–572. [CrossRef]
18. Zhang, X.W.; Zhang, L.F.; Yang, W.; Wang, Y.; Liu, Y.; Dong, Y.C. Characterization of the three-dimensional morphology and formation mechanism of inclusions in linepipe steels. *Metall. Mater. Trans. B* **2017**, *48*, 701–712. [CrossRef]
19. Zhang, X.W.; Zhang, L.F.; Yang, W.; Dong, Y.C. Characterization of MnS particles in heavy rail steels using different methods. *Steel Res. Int.* **2017**, *88*, 1600080. [CrossRef]
20. Zhang, D.; Shen, P.; Xie, J.B.; An, J.M.; Huang, Z.Z.; Fu, J.X. A method for observing tridimensional morphology of sulfide inclusions by non-aqueous solution electrolytic etching. *J. Iron Steel Res. Int.* **2019**, *26*, 275–284. [CrossRef]
21. Andersson, J. A thermodynamic evaluation of the Fe-Cr-C system. *Metall. Trans. A* **1988**, *19*, 627–636. [CrossRef]
22. Tian, Q.R.; Wang, G.C.; Shang, D.L.; Lei, H.; Yuan, X.H.; Wang, Q.; Li, J. In Situ Observation of the Precipitation, Aggregation, and Dissolution Behaviors of TiN Inclusion on the Surface of Liquid GCr15 Bearing Steel. *Metall. Mater. Trans. B* **2018**, *49*, 3137–3150. [CrossRef]
23. Li, B.; Shi, X.; Guo, H.J.; Guo, J. Study on Precipitation and Growth of TiN in GCr15 Bearing Steel during Solidification. *Materials* **2019**, *12*, 1463. [CrossRef] [PubMed]
24. Wang, Y.N.; Yang, J.; Bao, Y.P. Characteristics of BN precipitation and growth during solidification of BN free-machining steel. *Metall. Mater. Trans. B* **2014**, *45*, 2269–2278. [CrossRef]
25. Huang, Y.W.; Long, M.J.; Liu, P.; Chen, D.F.; Chen, H.B.; Gui, L.T.; Liu, T.; Yu, S. Effects of partition coefficients, diffusion coefficients, and solidification paths on microsegregation in Fe-based multinary alloy. *Metall. Mater. Trans. B* **2017**, *48*, 2504–2515. [CrossRef]
26. Miettinen, J. Thermodynamic-kinetic simulation of constrained dendrite growth in steels. *Metall. Mater. Trans. B* **2000**, *31*, 365–379. [CrossRef]
27. Ohnaka, I. Mathematical analysis of solute redistribution during solidification with diffusion in solid phase. *ISIJ Int.* **1986**, *26*, 1045–1051. [CrossRef]
28. Turnbull, D.; Vonnegut, B. Nucleation catalysis. *Ind. Eng. Chem.* **1952**, *44*, 1292–1298. [CrossRef]
29. Bramfitt, B.L. The effect of carbide and nitride additions on the heterogeneous nucleation behavior of liquid iron. *Metall. Trans.* **1970**, *1*, 1987–1995. [CrossRef]

30. Ding, M.Y.; Yang, Y.; Wu, B.S.; Li, Y.W.; Wang, T.J.; Ma, L.L. Study on reduction and carburization behaviors of iron-based Fischer-Tropsch synthesis catalyst. *Energy Procedia* **2014**, *61*, 2267–2270. [CrossRef]
31. Morniroli, J.P.; Gantois, M. Etude microstructurale de carbures M7C3. *J. Appl. Crystallogr.* **1983**, *16*, 1–10. [CrossRef]
32. Fruchart, D.; Chaudouet, P.; Fruchart, R.; Rouault, A.; Senateur, J.P. Etudes structurales de composés de type cémentite: Effet de l'hydroge'ne sur Fe3C suivi par diffraction neutronique. Spectrométrie Mössbauer sur FeCo 2B et Co 3B dopés au 57Fe. *J. Solid State Chem.* **1984**, *51*, 246–252. [CrossRef]
33. Descotes, V.; Bellot, J.P.; Witzke, S.; Jardy, A. Modeling the titanium nitride (TiN) germination and growth during the solidification of a maraging steel. In Proceedings of the 2013 International Symposium on Liquid Metal Processing & Casting, Austin, TX, USA, 22–25 September 2013; pp. 201–206.
34. Pervushin, G.V.; Suito, H. Precipitation behavior of TiN in Fe-10mass% Ni alloy during solidification and isothermal holding at 1400 °C. *ISIJ Int.* **2001**, *41*, 728–737. [CrossRef]
35. Shibata, H.; Yin, H.; Yoshinaga, S.; Emi, T.; Suzuki, M. In-situ observation of engulfment and pushing of nonmetallic inclusions in steel melt by advancing melt/solid interface. *ISIJ Int.* **1998**, *38*, 149–156. [CrossRef]

© 2019 by the authors. Licensee MDPI, Basel, Switzerland. This article is an open access article distributed under the terms and conditions of the Creative Commons Attribution (CC BY) license (http://creativecommons.org/licenses/by/4.0/).